Supplementary Information

MODELING HIERARCHICALLY STRUCTURED NANOPARTICLE/DIBLOCK COPOLYMER SYSTEMS

Zbyšek Posel,[a,#] *Paola Posocco,*[b,#] *Maurizio Fermeglia,*[b] *Martin Lísal,*[c,d] *and Sabrina Pricl*[b,e,*]

[a]Department of Informatics, Faculty of Science, J. E. Purkinje University, 400 96 Ústí nad Labem, Czech Republic. [b]Molecular Simulations Engineering (MOSE) Laboratory, Department of Engineering and Architecture (DEA), University of Trieste, via Valerio 10, 34127 Trieste, Italy. [c]Department of Physics, Faculty of Science, J. E. Purkinje University, 400 96 Ústí nad Labem, Czech Republic. [d]E. Hála Laboratory of Thermodynamics, Institute of Chemical Process Fundamentals of the ASCR, v. v. i., 165 02 Prague 6-Suchdol, Czech Republic. [e]National Interuniversity Consortium for Material Science and Technology (INSTM), Research Unit MOSE-DEA, University of Trieste, Italy

[#]These authors equally contributed to this work

TABLE OF CONTENTS

S1 - General phase diagram for diblock copolymers (DBCPs)

The first, general phase diagram for diblock copolymer was derived using self-consistent field theory (SCFT), and was limited to the classical lamellar (L), cylindrical (C), and *bcc* spherical (S) phases.[1] Matsen and Schick then extended it to include complex phases, predicting the gyroid (G) phase to be more stable than the perforated-lamellar (PL) phase[2] as confirmed later by experiment. In a subsequent calculation by Matsen and Bates,[3] a narrow closed-packed spherical (Scp) phase was predicted along the order-disorder transition (ODT), which has since been associated with a region of densely packed spherical micelles. Most recently, the *Fddd* (O^{70}) phase was predicted by Tyler and Morse[4] and later observed in experiment.[5,6,7]

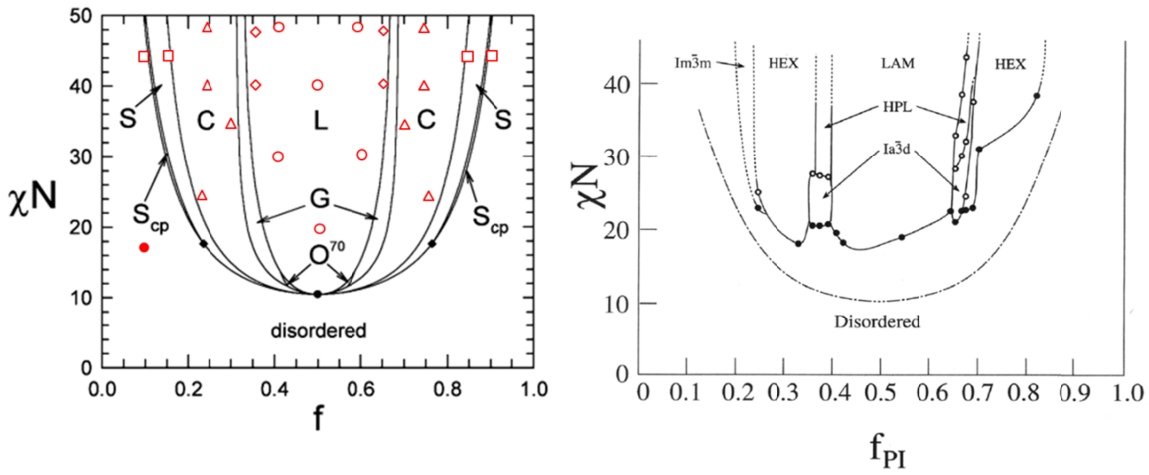

Scheme S1. (left) SCFT and simulation phase diagram for DBCP melt showing the stability regions of the lamellar (L), cylindrical (C), *bcc* spherical (S), hcp spherical (S_{cp}), gyroid (G), and *Fddd* (O^{70}) phases.[8] Results obtained from DPD[9,10] are indicated by red symbols. Symbols legend: circles, lamellae; triangles, hexagonally packed cylinders; diamonds, gyroid; squares, bcc ordered spheres; filled circles, disordered phase. (Right) An example of the experimental phase diagram of polyisoprene-polystyrene (PS-PI) diblock copolymer.[11] Redrawn with permission from Matsen, M. W. Effect of architecture on the phase behavior of AB-type block copolymer melts. *Macromolecules* **2012**, *45*, 2161−2165 and Khandpur, A. K.; Förster, S.; Bates, F. S.; Hamley, A. W.; Ryan, A. J.; Bras, W.; Almdal, K.; Mortensen, K. Polyisoprene-Polystyrene diblock copolymer phase diagram near the order-disorder transition. *Macromolecules* **1995**, *28*, 8796-8806. Copyright {2012} American Chemical Society.

S2 - Dissipative Particle Dynamics

In this work, we applied the Dissipative Particle Dynamics (DPD) simulation method. DPD is a particle-based mesoscale technique first introduced by Hoogerbrugge and Koelman [12] and cast in its present form by Español and Warren,[13] and Groot and Warren.[14] In DPD, a number of particles are coarse-grained into fluid elements, called *beads*. These DPD beads interact via pairwise additive interactions that locally conserve momentum, a necessary condition for a correct description of hydrodynamics,[15] while retaining essential information about the structural and physical-chemical properties of the system components. An advantageous feature of DPD is that it employs soft repulsive interactions between the beads, thereby allowing for larger integration time steps than in a typical molecular dynamics using for example Lennard-Jones interactions. Thus, time and length scales much larger (up to microseconds range) than those in atomistic molecular dynamics simulations can be accessed. Since its original derivation, the method has become a popular choice for the study of soft condensed matter, including DBCP,[16,17,18,19] polymer nanocomposites,[20,21] self-assembly of amphiphilic molecules,[22,23] polymer brushes,[24,25] lipid bilayers membranes,[26,27] just to name a few.

In DPD the beads move according to Newton's equations:

$$\frac{d\boldsymbol{r}_i}{dt} = \frac{\boldsymbol{p}_i(t)}{m_i} \quad \frac{d\boldsymbol{p}_i}{dt} = \boldsymbol{f}_i(t) \tag{1}$$

where $\boldsymbol{r}_i(t)$, $\boldsymbol{p}_i(t)$, m_i, and $\boldsymbol{f}_i(t)$ are the position, momentum, mass and net force and mass of particle i, respectively. $\boldsymbol{f}_i(t)$ is given as the sum of three different forces: a conservative force $\boldsymbol{F}_{ij}^{C}$, a dissipative force $\boldsymbol{F}_{ij}^{D}$, and a random force $\boldsymbol{F}_{ij}^{R}$:

$$\boldsymbol{f}_i = \sum_{i \neq j} \boldsymbol{F}_{ij} = \sum_{i \neq j} \boldsymbol{F}_{ij}^{C} + \boldsymbol{F}_{ij}^{D} + \boldsymbol{F}_{ij}^{R} \tag{2}$$

All forces are pairwise and lay along the line joining two interacting particles i and j. The conservative force for non-bonded beads $\boldsymbol{F}_{ij}^{C}$ represents a soft repulsion modeled as a linear

function of the distance between two particles, while the dissipative force $\boldsymbol{F}_{ij}^{D}$ slows down the particle motions, thus accounting for the effects of viscosity, and the random force $\boldsymbol{F}_{ij}^{R}$ provides the thermal or vibrational energy of the system. The dissipative force acts to reduce the relative momentum between beads *i* and *j*, while random force impels energy into the system. The expressions for the forces are given by the following equations:

$$\boldsymbol{F}_{ij}^{C} = a_{ij}\left(1 - \frac{r_{ij}}{r_c}\right)\frac{\boldsymbol{r}_{ij}}{r_{ij}} \tag{3}$$

$$\boldsymbol{F}_{ij}^{D} = -\gamma_{ij}\omega^{D}\left(r_{ij}\right)\left(\frac{\boldsymbol{r}_{ij}}{r_{ij}} \cdot \boldsymbol{v}_{ij}\right)\frac{\boldsymbol{r}_{ij}}{r_{ij}} \tag{4}$$

$$\boldsymbol{F}_{ij}^{R} = \sigma_{ij}\omega^{R}\left(r_{ij}\right)\frac{\zeta_{ij}}{\sqrt{\Delta t}}\frac{\boldsymbol{r}_{ij}}{r_{ij}} \tag{5}$$

where a_{ij} is the maximum repulsion parameter between particle *i* and *j*, $\boldsymbol{r}_{ij} = \boldsymbol{r}_i - \boldsymbol{r}_j$ is the vector joining beads *i* and *j*, $r_{ij} = |\boldsymbol{r}_{ij}|$ is the distance between particle *i* and *j*, $\boldsymbol{v}_{ij} = \boldsymbol{v}_i - \boldsymbol{v}_j$ is the relative velocity, and $\boldsymbol{v}_i = \boldsymbol{p}_i/m_i$. All the above forces acts within the cut-off radius r_c, which basically constitutes the length scale of the entire system. γ_{ij} is a friction coefficient, σ_{ij} the noise amplitude, ζ_{ij} a Gaussian random number with a zero mean and a unit variance chosen independently for each pair of particles, and Δt is the time step in the simulation. $\omega^{D}(r_{ij})$ and $\omega^{R}(r_{ij})$ are weight functions vanishing for distance greater than r_c. Español and Warren[13] showed that the system samples the canonical ensemble and obeys the fluctuation-dissipation theorem if the following conditions are satisfied:

$$w^{D}\left(r_{ij}\right) = \left[w^{R}(r_{ij})\right]^{2} \tag{6}$$

$$\sigma_{ij}{}^{2} = 2\gamma_{ij}k_B T \tag{7}$$

where *T* is the temperature and k_B is the Boltzmann constant and $\omega^{D}(r_{ij})$ and $\omega^{R}(r_{ij})$ are typically chosen as:[14]

$$w^D(r_{ij}) = \left[w^R(r_{ij})\right]^2 = \begin{cases} \left(1 - r_{ij}/r_c\right)^2 & r_{ij} < r_c \\ 0 & r_{ij} \geq r_c \end{cases} \quad (8)$$

Finally, when modeling polymers, another force, in addition to those defined in Eq. (2), is active in the system, i.e., the harmonic spring connecting the adjacent particles:

$$\boldsymbol{F}_{ij}^{spring} = K\left(\boldsymbol{r}_{ij} - \boldsymbol{r}_0\right) \quad (9)$$

where K is the spring constant and r_0 is the equilibrium distance between two adjacent particles i and j.

Structure and nanoparticle distribution analysis

We monitored the orientation order parameter (OOP) during the equilibration period to identify order and disorder states. The OOP is the ensemble average of largest eigenvalue of Saupe tensor.[28] Once the OOP reached a plateau value, we considered the structure as ordered, i.e. equilibrated. Further, the thermodynamic stability could be discerned from equality of the diagonal components of the pressure tensor. According to Schultz et al.,[29] the system with equal pressure in each direction is the system with the lowest free energy. Figure S1 shows the evolution of the OOP for PS_7PVP_{13} (f = 0.35) gyroid matrix as a function of simulation time step, taken as a proof of concept. The red dashed line highlights the plateau value.

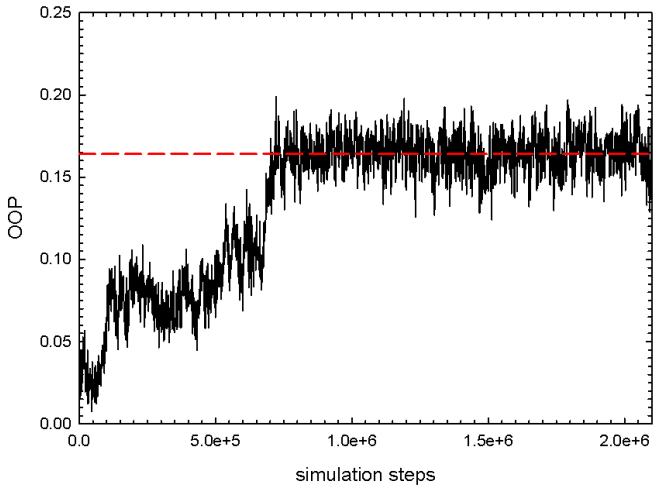

Figure S1. Orientation order parameter (OOP) as a function of simulation steps for PS_7PVP_{13} gyroid morphology. The red dashed line indicates the plateau value.

To distinguish between well-ordered and not well-ordered structure we derived the structure factor $S(\boldsymbol{q})$ from simulation using the following relationship:[30]

$$S(\boldsymbol{q}) = \frac{(\sum_j \cos(\boldsymbol{q}\cdot\boldsymbol{r}_j))^2+(\sum_j \sin(\boldsymbol{q}\cdot\boldsymbol{r}_j))^2}{N} \quad (10)$$

where $\boldsymbol{q}$ is the wave vector and $\boldsymbol{r}_j$ is the position of jth particle of type *PS* or *PVP*. Structure factors $S(\boldsymbol{q})$ calculated from well-ordered matrices were compared to those obtained in the presence of NPs.

Further, we employed Voronoi tessellation[31] and estimated the list of nearest neighbors (NNs) for each particle in the system. For a set of DPD beads in a system, the tessellation is defined by associating a cell of space to each bead, that corresponds to the section of the system which is closer to that bead than any other. The Voronoi diagram perfectly partitions the system, and it is used in problems that involve allocating space between a group of objects.[32] For constructing the Voronoi polyhedra we employed the free software Voro++.[33] Considering an

independent cluster as an ensemble of NNs of type *PS*/*PVP*, we obtained and distinguished particular spheres, cylinders or lamellar planes. For every cluster we computed its center-of-mass (COM) as:

$$\boldsymbol{r}_{COM} = \frac{\sum_i m_i \boldsymbol{r}_i}{\sum_i m_i} \tag{11}$$

Cluster size and shape were determined from the cluster gyration tensor R_g^2 and shape anisotropy κ^2, respectively. The mean-squared radius of gyration R_g^2 is defined as:

$$R_g^2 = \lambda_x^2 + \lambda_y^2 + \lambda_z^2 \tag{12}$$

while the related shape anisotropy κ^2 is given by:

$$\kappa^2 = \frac{b^2 + (3/4)c^2}{R_g^4} \tag{13}$$

where $\lambda_{x,y,z}^2$ are the principal moments of the cluster gyration tensor and b and c are the asphericity and acylindricity of the cluster, respectively,[34,35] and expressed as:

$$\mathrm{b} = \lambda_z^2 - \frac{1}{2}\left(\lambda_x^2 + \lambda_y^2\right) \tag{14}$$

$$\mathrm{c} = \lambda_y^2 - \lambda_x^2 \tag{15}$$

To specify the location of the NPs in a given system we calculated the distribution of NNs of *PS* and *PVP* type around every segment of a NP. The list of the NNs was again obtained by Voronoi analysis. The corresponding percentage of *PS* and *PVP* segments was then estimated from the total number of NNs for every segment of the nanoparticle. Thus, for example, if a NP decoration contains more *PS* than *PVP* oligomers, it will be prevalently located in a PS domain of the DBCP matrix and will have more NNs of the *PS* type. This reflects in the presence of peaks at higher percentage of NNs of the *PS* type in the corresponding distribution curve of the NNs. If the NP coverage is composed by an equal amount of *PS* and *PVP* chains, the distribution

curve for *PS* and *PVP* segment type is similar, as intuitively expected. However, depending of the relative size of the spheres/cylinders and the size of the NP, peaks at higher percentage of NNs for *PVP* can be observed, even if the nanoparticle is prevalently or fully located in a *PS* domain (see main text for discussion).

In the presence of an hexagonal morphology where the cylinder length is the dominant dimension additional steps was performed before obtaining the NPs distribution. Every cylinder, represented as a cluster of nearest neighbors of *PS* type, was divided into cylindrical subdomains. Every subdomain has the same diameter as the original cylinder with a shorter cylinder length. The analysis was performed on the subdomains and averaged over many independent configurations. The reason for this procedure is that the analysis of cylindrical subdomains (e.g., radius of gyration R_g) gives better results when the nanoparticles are included into the domain while the analysis of the original, whole cylinder can be smeared out by the dominant dimension.

Supplementary results

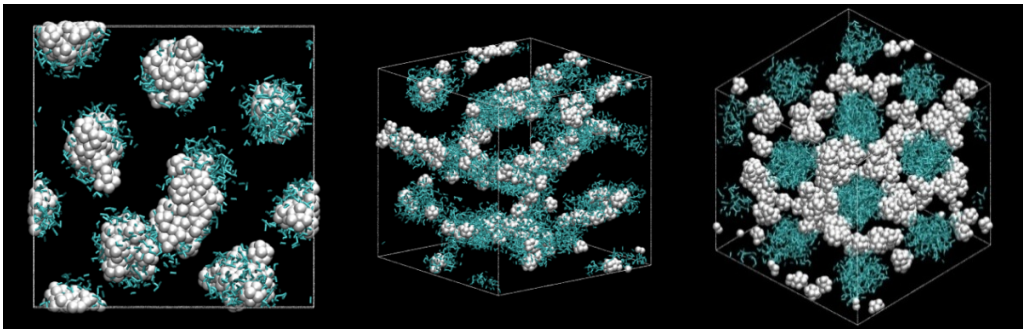

(a) (b) (c)

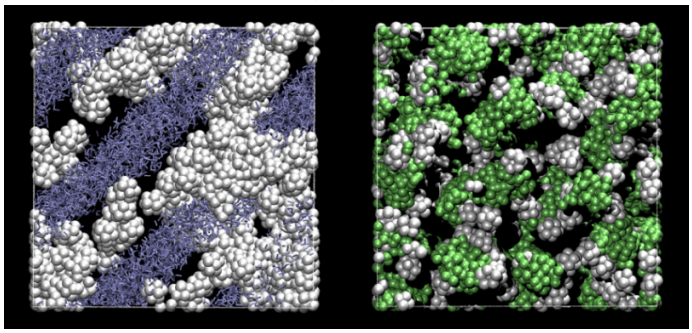

(d) (e)

Figure S2. Effect of NP loading on DBCP morphology. (a) DBCP composition, PS_4PVP_{16} (f = 0.2); NP volume fraction, V_f = 0.05; NP coverage, *PS*. The pristine hexagonal cylindrical structure evolved into not well ordered spheres. (b) DBCP composition, PS_6PVP_{14} (f = 0.3); NP volume fraction, V_f = 0.03; NP coverage, PS_9PVP_3. Not well ordered hexagonal packing was observed. (c) DBCP composition, PS_6PVP_{14} (f = 0.3); NP volume fraction, V_f = 0.05; NP coverage, *PVP*. The pristine hexagonal cylindrical structure is fully preserved and NPs accommodate in the *PVP* domain surrounding the *PS* cylinders. (d) DBCP composition, PS_8PVP_{12} (f = 0.4); NP volume fraction, V_f = 0.1; NP coverage, *PVP*. NP aggregation crossing the *PS* domain and holing the lamella occurs. (e) DBCP composition, PS_2PVP_{18} (f = 0.1); NP volume fraction, V_f = 0.05; NP coverage, PS_3PVP_9. NPs place at the interface between the domains bridging the *PS* spheres. Legend: *PS* domain is represented as cyan sticks in (a)-(c) panels, iceblue sticks in (d) panel, lime spheres in (e) panel; NPs are represented as white spheres. *PVP* domain is omitted for clarity.

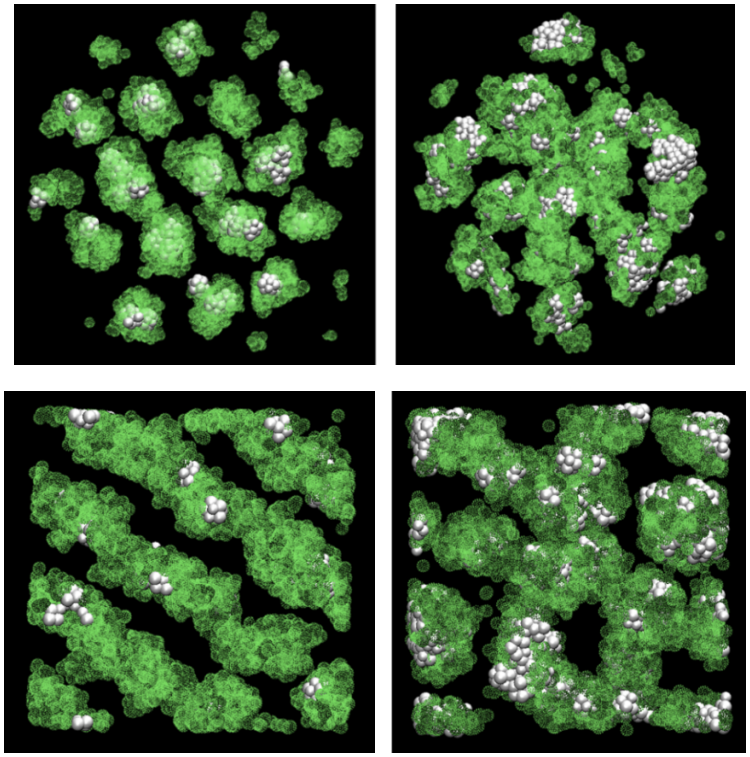

Figure S3. Effect of nanofiller loading in a PS_2PVP_{18} (f = 0.1). Coverage composition corresponds to PS_9PVP_3. Perfect *bcc* structure is observed at NPs V_f= 0.01 (left panels) and imperfect *bcc* structure at V_f = 0.05 (right panels). *bcc* lattice is displayed from different crystallographic planes in top and bottom panels. Legend: *PS* domain is represented as dotted green spheres and NPs as white spheres. *PVP* domain is omitted for clarity.

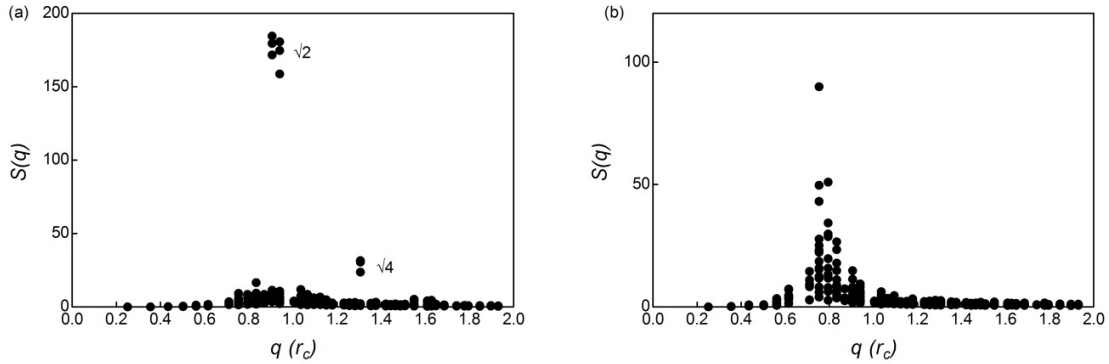

Figure S4. Structure factor calculated from simulation of *PS* block in a spherical matrix PS_2PVP_{18} (f = 0.1) and at NP coverage equal to PS_9PVP_3 for 0.01 (a) and 0.05 (b) NP V_f. At low V_f peaks nicely correspond to a perfect bcc organization, while no ordering was observed at higher concentration.[36]

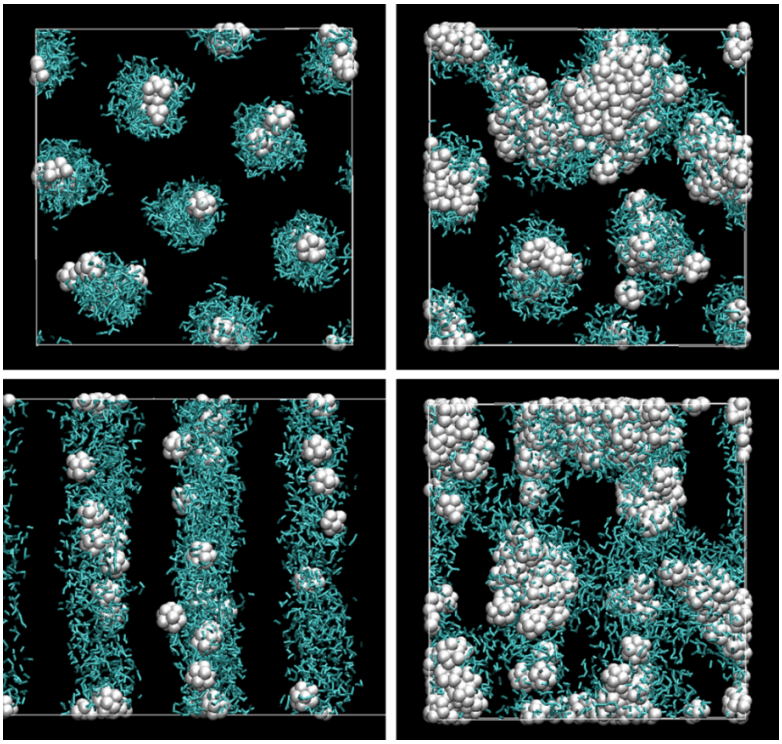

Figure S5. Effect of nanofiller loading in a PS_5PVP_{15} (f = 0.25). NP coverage composition corresponds to $PS_{11}PVP_1$. Hexagonal ordered structure is observed at NPs V_f = 0.01 (left panels) and not ordered structure at V_f = 0.05 (right panels). Legend: *PS* domain is represented as cyan sticks and NPs as white spheres. *PVP* domain is omitted for clarity.

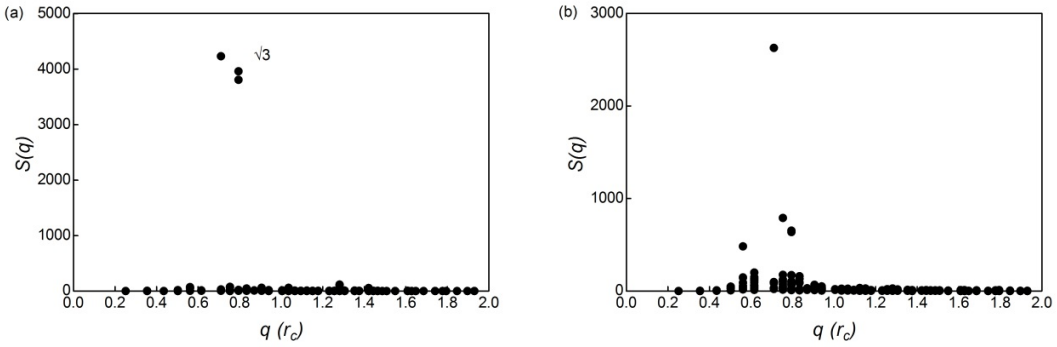

Figure S6. Structure factor calculated from simulation snapshots of *PS* block in a PS_5PVP_{15} (f = 0.25) copolymer and at NP coverage equal to $PS_{11}PVP_1$ for 0.01 (a) and 0.05 (b) NP concentration. At low V_f peaks evidence an hexagonal cylinder phase, while no ordering was observed at higher concentration.[36]

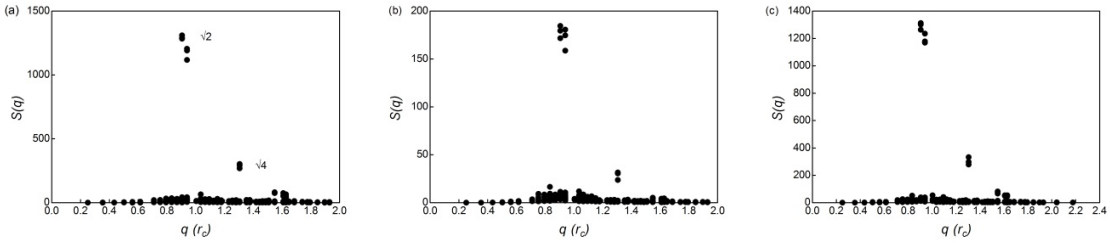

Figure S7. Structure factor calculated from simulation snapshots of *PS* block for a spherical matrix PS_2PVP_{18} (f = 0.1) (a), filled with PS_9PVP_3 (b) and PS_1PVP_{11} (c) NPs at a volume fraction V_f = 0.01. Diagrams (b) and (c) demonstrate that the addition of NPs at this V_f does not alter the bcc ordering of the DBCP matrix.

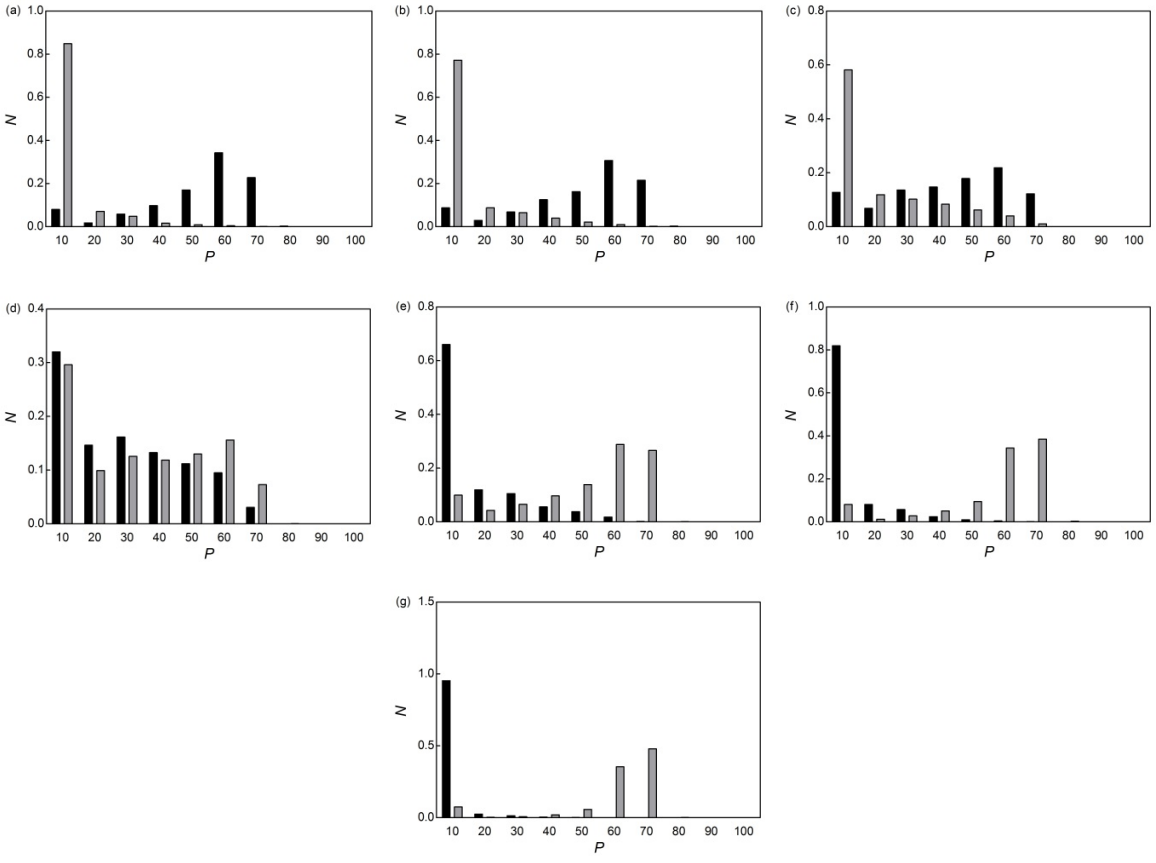

Figure S8. Distribution of the NNs of PS and PVP *N* type located around every segment of NP in the case of a spherical matrix PS_2PVP_{18} (f = 0.1) at V_f = 0.01 for the following coverage: (a) *PS*; (b) $PS_{11}PVP_1$; (c) PS_9PVP_3; (d) PS_6PVP_6; (e) PS_3PVP_9; (f) PS_1PVP_{11}; (g) *PVP*. *P* represents the percent ratio of *PS* or *PVP* NN with respect to the total amount of NNs located around every segment of NP. Legend: black bar, *PS*; grey bar, *PVP*.

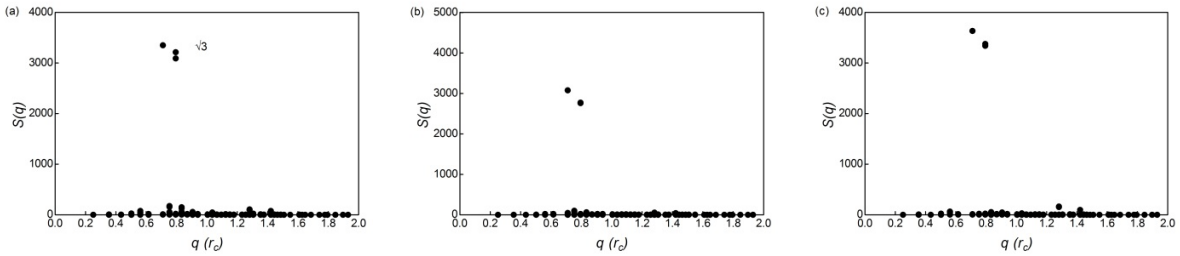

Figure S9. Structure factor calculated from simulation snapshots of *PS* block for a cylindrical matrix PS_5PVP_{15} (f = 0.25) (a), filled with PS_9PVP_3 (b), and PS_1PVP_{11} (c) NPs at a volume fraction V_f = 0.03. Diagrams (b) and (c) demonstrate that the addition of NPs at this V_f does not alter the bcc ordering of the DBCP matrix.

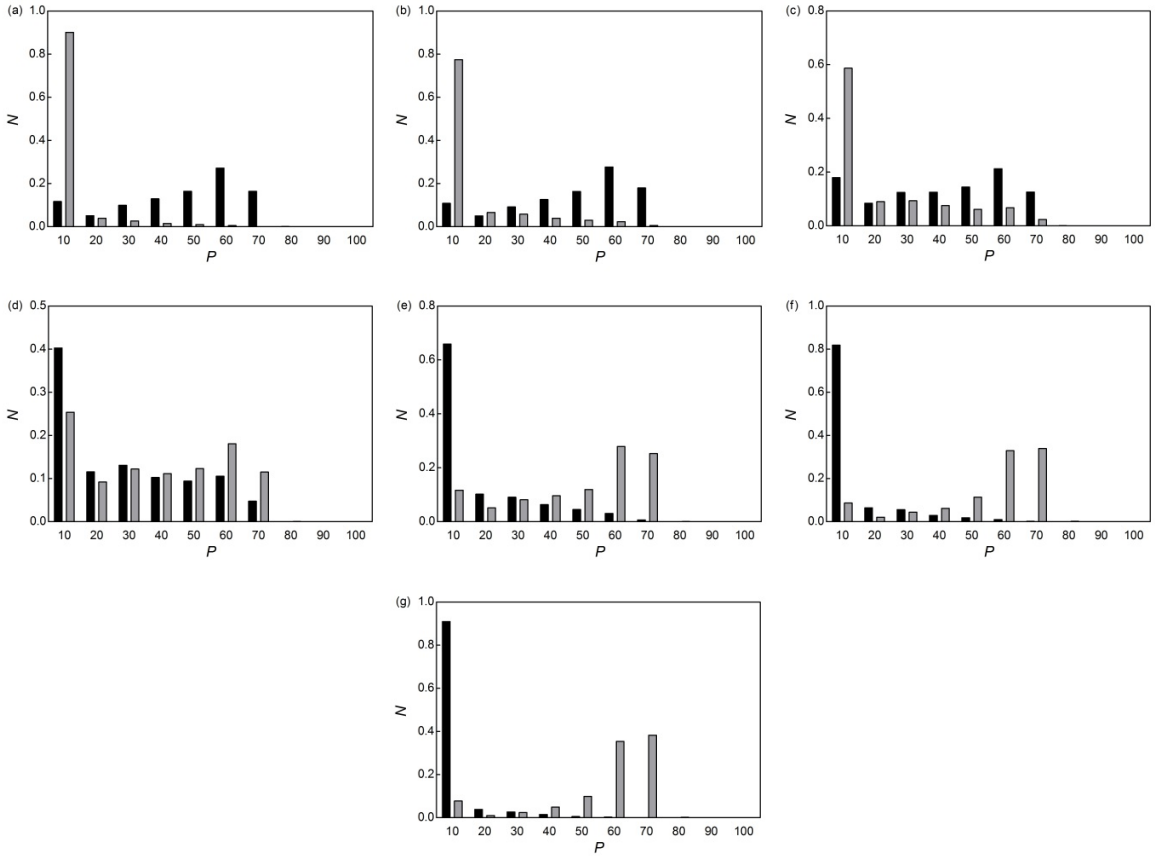

Figure S10. Distribution of the NNs of PS and PVP *N* type located around every segment of NP in the case of a hexagonally packed structure PS_5PVP_{15} (f = 0.25) at V_f = 0.03 for the following coverage: (a) *PS*; (b) $PS_{11}PVP_1$; (c) PS_9PVP_3; (d) PS_6PVP_6; (e) PS_3PVP_9; (f) PS_1PVP_{11}; (g) *PVP*. *P* represents the percent ratio of *PS* or *PVP* NNs with respect to the total amount of NNs located around every segment of NP. Legend: black bar, *PS*; grey bar, *PVP*.

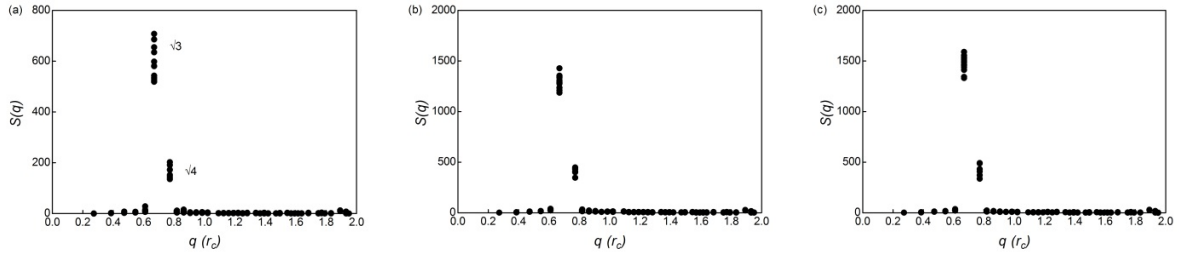

Figure S11. Structure factor calculated from simulation snapshots of *PS* block in a gyroid matrix PS_7PVP_{13} ($f = 0.35$) (a) filled with $PS1_9PVP_3$ (b) and $PS1_1PVP_{11}$ (c) NPs at a volume fraction $V_f = 0.03$. It is noteworthy that the DBCP conformation is not affect by the presence of NPs as shown by the comparison of the peaks in the structure factor diagrams reported.[37]

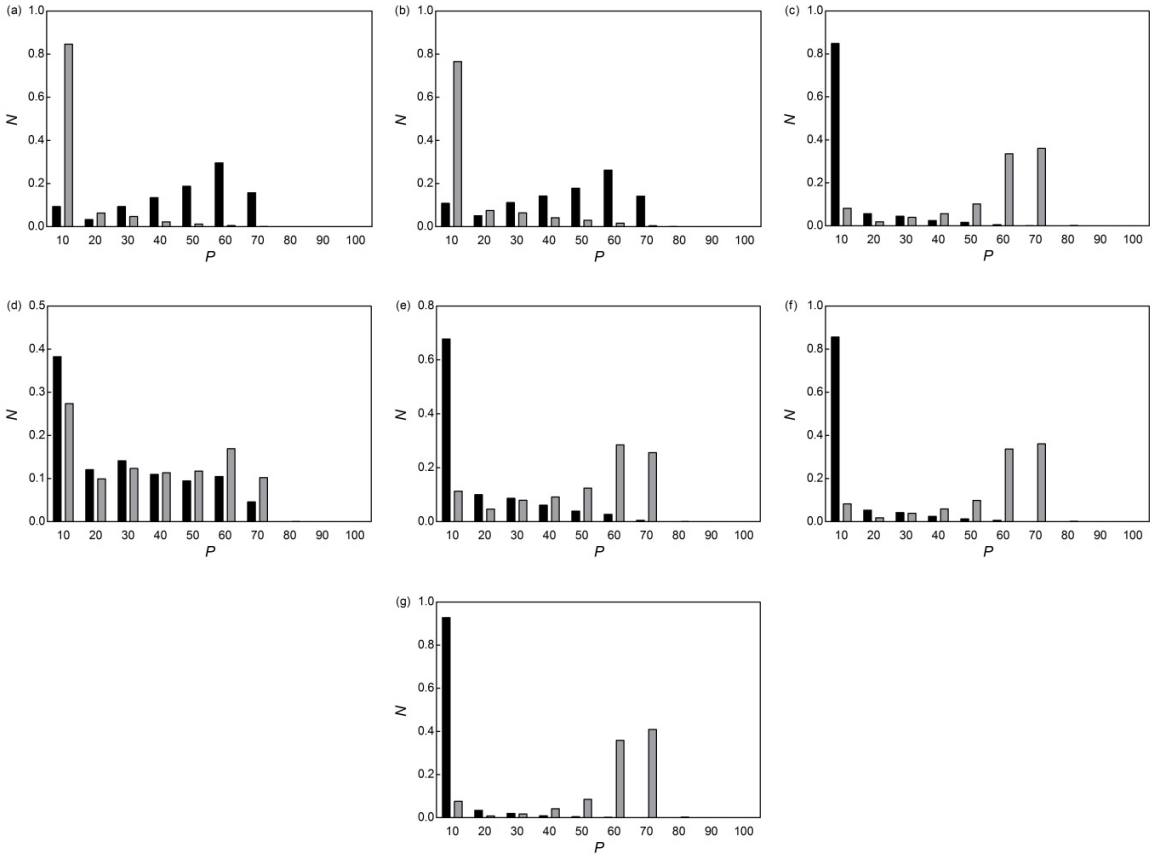

Figure S12. Distribution of the NNs of PS and PVP *N* type located around every segment of NP in the case of a hexagonally packed structure PS_4PVP_{16} ($f = 0.2$) at $V_f = 0.03$ for the following coverage: (a) *PS*; (b) $PS_{11}PVP_1$; (c) PS_9PVP_3; (d) PS_6PVP_6; (e) PS_3PVP_9; (f) PS_1PVP_{11}; (g) *PVP*. *P* represents the percent ratio of *PS* or *PVP* NNs with respect to the total amount of NNs located around every segment of NP. Legend: black bar, *PS*; grey bar, *PVP*.

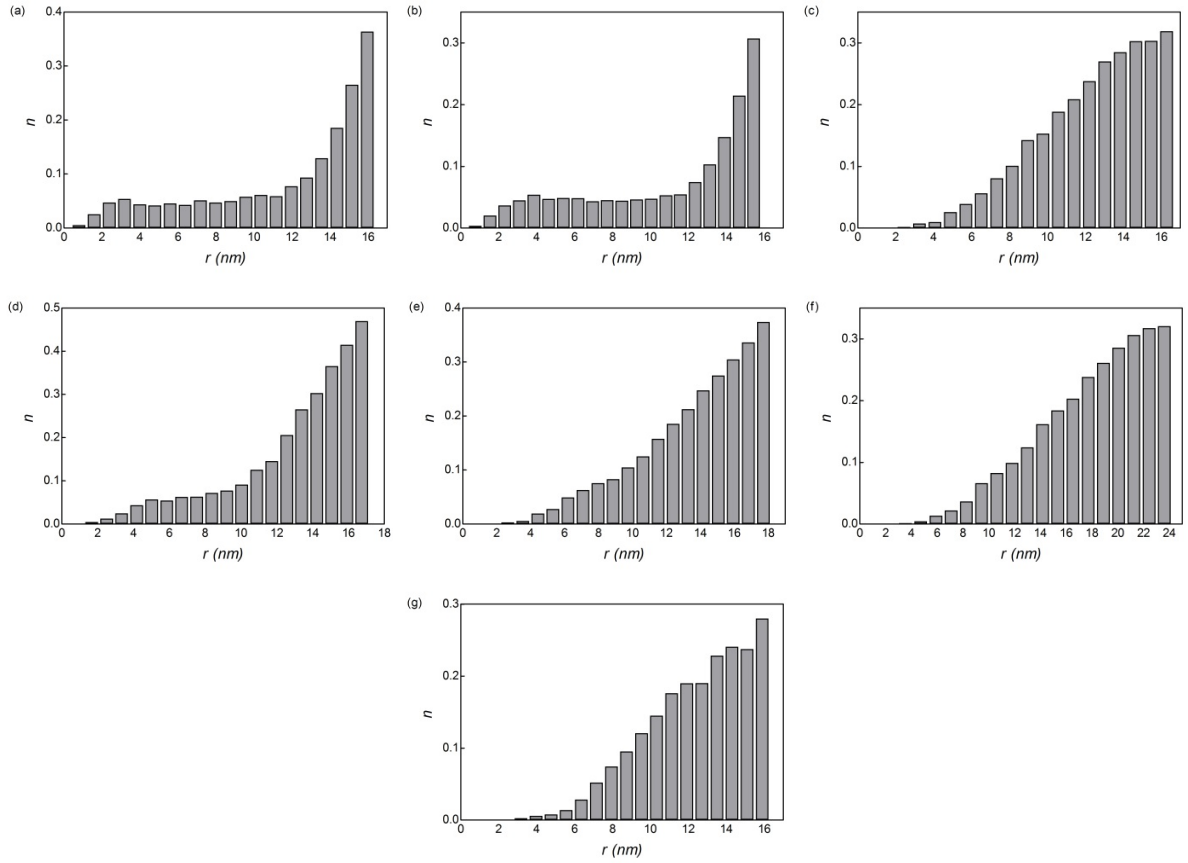

Figure S13. Distribution of NPs n as a function of distance r from the center of mass of the cylindrical sub-domains in the case of a PS_4PVP_{16} (f = 0.2) at V_f = 0.03 for the following coverage: (a) PS; (b) $PS_{11}PVP_1$; (c) PS_9PVP_3; (d) PS_6PVP_6; (e) PS_3PVP_9; (f) PS_1PVP_{11}; (g) PVP.

References

1 J. D. Vavasour and M. D. Whitmore Self-Consistent Mean Field Theory of the Microphases of Diblock Copolymers *Macromolecules*, 1992, **25**, 5477-5486.

2 M. W. Matsen and M. Schick Stable and unstable phases of a diblock copolymer melt *Phys. Rev. Lett.*, 1994, **72**, 2660-2663.

3 M. W. Matsen and F. S. Bates Unifying Weak- and Strong-Segregation Block Copolymer Theories *Macromolecules*, 1996, **29**, 1091-1098.

4 C. A. Tyler and D. C. Morse The orthorhombic *Fddd* network in triblock and diblock copolymer melts *Phys. Rev. Lett.*, 2005, **94**, 208302.

5 M. Takenaka, T. Wakada, S. Akasaka, S. Nishitsuji, K. Saijo, H. Shimizu, M. I. Kim and H. Hasegawa Orthorhombic *Fddd* Network in Diblock Copolymer Melts *Macromolecules*, 2007, **40**, 4399-4402.

6 M. I. Kim, T. Wakada, S. Akasaka, S. Nishitsuji, K. Saijo, H. Hasegawa, K. Ito and M. Takenaka Stability of the *Fddd* Phase in Diblock Copolymer Melts *Macromolecules*, 2008, **41**, 7667-7670.

7 M. I. Kim, T. Wakada, S. Akasaka, S. Nishitsuji, K. Saijo, H. Hasegawa, K. Ito and M. Takenaka Determination of the *Fddd* Phase Boundary in Polystyrene-block-polyisoprene Diblock Copolymer Melts *Macromolecules*, 2009, **42**, 5266-5271.

8 Matsen, M. W. Effect of architecture on the phase behavior of AB-type block copolymer melts. *Macromolecules* **2012**, *45*, 2161−2165.

9 Groot, R. D.; Madden, T. J.; Tildesley, D. J. On the role of hydrodynamic interactions in block copolymer microphase separation. *J. Chem. Phys.* **1999**, 110, 19, 9739-9749.

10 Martínez-Veracoechea, F. J.; Escobedo, F. A. Simulation of the gyroid phase in off-lattice models of pure diblock copolymer melts. *J. Chem. Phys.* **2006**, 125, 104907.

11 Khandpur, A. K.; Förster, S.; Bates, F. S.; Hamley, A. W.; Ryan, A. J.; Bras, W.; Almdal, K.; Mortensen, K. Polyisoprene-Polystyrene Diblock Copolymer Phase Diagram near the Order-Disorder Transition. *Macromolecules* **1995**, 28, 8796-8806.

12 Hoogerbrugge, P. J.; Koelman, J. M. V. A. Simulating microscopic hydrodynamic phenomena with dissipative particle dynamics. Europhys. Lett. 1992, 19, 155-160.

[13] Español, P.; Warren, P. Statistical mechanics of dissipative particle dynamics. *Europhys. Lett.* **1995,** *30,* 191-196.

14 Groot, R.; Warren, P. B. Dissipative particle dynamics: bridging the gap between atomistic and mesoscopic simulation. *J. Chem. Phys.* **1997,** *107,* 4423–4435.

15 Ripoll, M.; Ernst, M. H.; Espanol, P. Large scale and mesoscopic hydrodynamics for dissipative particle dynamics. *J. Chem. Phys.* **2001,** *115,* 7271-7284.

16 Groot, R. D.; J., M. T. Dynamic simulation of diblock copolymer microphase separation. *J. Chem. Phys.* **1998,** *108,* 8713-8724.

17 Roy, S.; Markova, D.; Kumar, A.; Klapper, M.; Müller-Plathe, F. Morphology of phosphonic acid-functionalized block copolymers studied by dissipative particle dynamics. *Macromolecules* **2009,** *42,* 841-848.

18 Petrus, P.; Lísal, M.; Brennan, J. K. Self-assembly of lamellar- and cylinder-forming diblock copolymers in planar slits: Insight from dissipative particle dynamics simulations. *Langmuir* **2010,** *26,* 14680–14693.

19 Kriksin, Y. A.; Khalatur, P. G.; Neratova, I. V.; Khokhlov, A. R.; Tsarkova, L. A. Directed assembly of block copolymers by sparsely patterned substrates. *J. Phys. Chem. C* **2011,** *115,* 25185–25200.

20 Posocco, P.; Posel, Z.; Fermeglia, M.; Lísal, M.; Pricl, S. A molecular simulation approach to the prediction of the morphology of self-assembled nanoparticles in diblock copolymers. *J. Mater. Chem.* **2010,** *20,* 10511-10520.

21 Toth, R.; Santese, F.; Pereira, S. P.; Nieto, D. R.; Pricl, S.; Fermeglia, M.; Posocco, P. Size and shape matter! A multiscale molecular simulation approach to polymer nanocomposites. *J. Mater. Chem.* **2012,** *22,* 5398-5409.

22 Li, Z.; Dormidontova, E. E. Kinetics of diblock copolymer micellization by dissipative particle dynamics. *Macromolecules* **2010,** *43,* 3521–3531.

23 Shillcock, J. C. Spontaneous vesicle self-assembly: a mesoscopic view of membrane dynamics. *Langmuir* **2012,** *28,* 541–547.

24 Goujon, F.; Malfreyt, P.; Tildesley, D. J. Mesoscopic simulation of entangled polymer brushes under shear: compression and rheological properties. *Macromolecules* **2009,** *42,* 4310–4318.

25 Goujon, F.; Ghoufi, A.; Malfreyt, P.; J., T. D. Frictional forces in polyelectrolyte brushes: effects of sliding velocity, solvent quality and salt. *Soft Matter* **2012,** *8,* 4635-4644.

26 Gao, L.; Shillcock, J.; Lipowsky, R. Improved dissipative particle dynamics simulations of lipid bilayers. *J. Chem. Phys.* **2007,** *126,* 015101-015108.

27 Rodgers, J. M.; Sørensen, J.; de Meyer, F. J.-M.; Schiøtt, B.; Smit, B. Understanding the phase behavior of coarse-grained model lipid bilayers through computational calorimetry. *J. Phys. Chem.* **2012,** *116,* 1551–1569.

28 De Gennes, P. G. and Prost, J. *The Physics of Liquid Crystals*; Oxford : Clarendon Press, 1993.

29 Schultz, A. J., Hall, C. K. and Genzer, J. Box length search algorithm for molecular simulation of system containing periodic structure. *J. Chem. Phys* **2004**, *120*, 2049.

30 McGreevy, R. L. *Computer Modeling in Inorganic Crystallography;* Academic Press: San Diego, CA, 1997.

31 Voronoi, G. Nouvelles applications des paramètres continus à la theorie des formes quadratiques. *Journal für die Reine und Angewandte Mathematik* **1907,** *133,* 97–178.

[32] M. P. Allen and D. J. Tildesley, Computer Simulation of Liquids, 2nd ed. (Oxford, Clarendon Press, 1987).

33 Chris Rycroft, H.; Grest, G. S.; Landry, J. W.; Bazant, M. Z. Analysis of granular flow in a pebble-bed nuclear reactor. *Phys. Rev. E* **2006,** *74,* 021306-021323.

34 Mattice, W.; UW, S. *Conformational Theory of Large Molecules;* Wiley Interscience: New York, NY, 1994.

35 Theodorou, D. N.; Suter, U. W. Shape of unperturbed linear polymers: polypropylene. *Macromolecules* **1985,** *18,* 1206–1214.

36 De Graef, M.; McHenry, M. E. *Structure of Materials: an Introduction to Crystallography, Diffraction, and Symmetry;* Cambridge University Press: Cambridge, 2007.

[37] Martınez-Veracoechea, F. J.; Escobedo, F. A. Lattice Monte Carlo simulations of the gyroidp phase in monodisperse and bidisperse block copolymer systems. *Macromolecules* **2005,** *38,* 8522 - 8531.